Steel and Composite Structures, *Vol. 26, No. 6 (2018) 793-808*
DOI: https://doi.org/10.12989/scs.2018.26.6.793

Experimental seismic behaviour of L-CFST column to H-beam connections

Wang Zhang [2], Zhihua Chen [*1,2,3], Qingqing Xiong [2,6], Ting Zhou [4], Xian Rong [5] and Yansheng Du [5]

[1] *State Key Laboratory of Hydraulic Engineering Simulation and Safety, China*
[2] *School of Civil Engineering, Tianjin University, Tianjin, China*
[3] *Key Laboratory of Coast Civil Structure Safety of China Ministry of Education, Tianjin, China*
[4] *School of Architecture, Tianjin University, Tianjin, China*
[5] *School of Civil and Transportation Engineering, Hebei University of Technology, Tianjin, 300401, China*
[6] *School of Civil Engineering, Shijiazhuang Tiedao University, Shijiazhuang, 050043, China*

(*Received September 4, 2017, Revised December 17, 2017, Accepted January 20, 2018*)

Abstract. In this study, the seismic performance of the connections between L-shaped columns composed of concrete-filled steel tubes (L-CFST columns) and H-beams used in high-rise steel frame structures was investigated. Seven full-scale specimens were tested under quasi-static cyclic loading. The variables studied in the tests included the joint type, the axial compression ratio, the presence of concrete, the width-to-thickness ratio and the internal extension length of the side plates. The hysteretic response, strength degradation, stiffness degradation, ductility, plastic rotation capacity, energy dissipation capacity and the strain distribution were evaluated at different load cycles. The test results indicated that both the corner and exterior joint specimens failed due to local buckling and crack within the beam flange adjacent to the end of the side plates. However, the failure modes of the interior joint specimens primarily included local buckling and crack at the end plates and curved corners of the beam flange. A design method was proposed for the flexural capacity of the end plate connection in the interior joint. Good agreement was observed between the theoretical and test results of both the yield and ultimate flexural capacity of the end plate connection.

Keywords: L-shaped column composed of concrete-filled steel tubes; side plate connection; end plate connection; experimental study; seismic performance; high-rise steel structure residential building; flexural capacity

1. Introduction

Given that special-shaped concrete-filled steel tube columns can be wrapped into walls, this type of construction facilitates indoor space conservation and convenient furniture arrangement. The object of investigation in this paper is the structural system of L-shaped columns composed of concrete-filled steel tubes (L-CFST) applied in high-rise steel-structure houses. In the high-rise steel structural system, the connections between the L-CFST columns and the H-beams can be used as corner, exterior and interior joints.As an important structural component, a joint can transmit and allocate internal forces in the frame structural system, which ensures structural integrity. The internal-diaphragm connection (Kang *et al*. 2015, Rezaifar and Younesi 2016, Nie *et al*. 2009), external-diaphragm connection (Lee *et al*. 2010, Vulcu *et al*. 2017), and through-diaphragm connection (Qin *et al*. 2016, Rong *et al*. 2016) have attracted broad research attention and are extensively used in many Asian countries for their outstanding economic and applicable performance. The strengthened beam flange connections and the reduced beam section connections are often adopted in engineering for achieving the purpose of steel beam plastic hinge away from the panel zone. In order to achieve the purpose of easier construction, the drilled flange connection is also proposed. Jazany and Ghobadi (2017) has used the experimentally validated detailed finite element models to study the cyclic responses of this novel reduced beam section connection.

In a high-rise residential structural system composed of L-CFST columns, the section width of a mono-column is generally 150 mm, which is not conducive to welding construction in the region of internal-diaphragm connection and is unfavourable to pouring concrete in the mono-column both for the internal-diaphragm connection and the through-diaphragm connection. In addition, the external-diaphragm connection affects the living space and aesthetics. Based on the above reasons, the side plate connection serves as an ideal connection form.

Currently, limited research exists on the seismic behaviour of side plate connections. Shin *et al*. (2008) conducted cyclic loading tests on seven square concrete-filled tube column-to-beam connections reinforced by T-shaped stiffeners. The results demonstrated that the tapered horizontal stiffener elements, RBS cut-outs and horizontal stiffener holes were effective in reducing the stress concentration at the tip of the horizontal element. Ghobadi *et al*. (2009a) analytically and experimentally investigated the development of the ductile detail of a T-stiffener added to existing moment connections. A fillet weld was ultimate as a replacement for a CJP groove weld in joining the T-stiffener to a beam flange. The results indicated that the crack propagation was eliminated using the new proposed

*Corresponding author, Professor,
E-mail: zhchen@tju.edu.cn

Copyright © 2018 Techno-Press, Ltd.

ISSN: 1229-9367 (Print), 1598-6233 (Online)

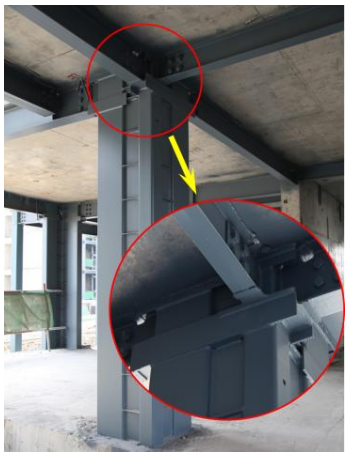

Fig. 1 Building using L-CFST columns under construction

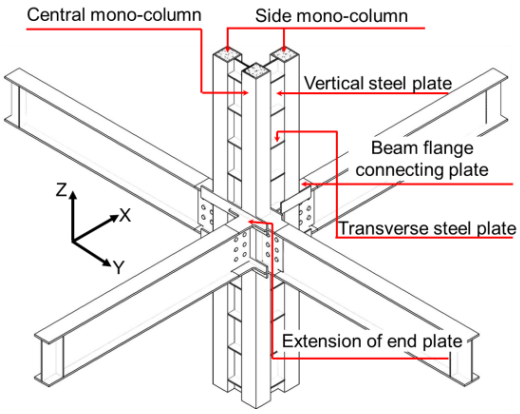

Fig. 2 Schematic diagram of the interior joint

procedure. Ma *et al*. (2017) conducted cyclic loading tests on two full-scale flange-reinforced connections between wide-flange specially-shaped composite columns and beams. The test results showed that cracks within the beam flanges occurred at the end of the reinforcement. In addition, there was no significant deformation of the panel zone. Zhao *et al*. (2017) and Zhou *et al*. (2015) experimentally investigated the behaviour of side plate connections to L-CFST column frames with and without a chevron concentric brace. Because the scale models were used in the frame tests, the seismic test results cannot represent the actual mechanical behaviour of the side plate connections.

An eighteen-story building with a height of 52.1 m that uses L-CFST columns for construction is presented in Fig. 1. The L-CFST column frame-brace structural system is adopted in this building. The majority of the frame columns are L-CFST columns. The ordinary rectangular concrete-filled steel tube columns are also used at the position that is difficult to arrange special-shaped columns. The system selects two bracing forms: cross RHS bracings and chevron RHS bracings. A steel-bar truss deck is also adopted in this building. The test results in this paper supply experimental support and the background for further parametric numerical analysis and seismic optimization analyses of this new type of structural system.

2. Experimental program

2.1 Specimen design

The interior joint in an L-CFST column structural system is presented in Fig. 2. In this case, the connections along the +X, +Y and -Y directions are side plate connections. The connection along the -X direction is an end-plate connection. When used as exterior joints, side plate connections only exist in the Y-Z plane. When used as corner joints, side plate connections only exist along the +X and -Y directions.

To study the influences on the seismic behaviour of the L-CFST column to H-beam connections, three groups of seven full-scale specimens were designed, including three corner joint specimens, two exterior joint specimens and two interior joint specimens. The test comparison parameters included the joint type, the axial compression ratio (n_0), the presence of concrete, the width-to-thickness ratio of side plate (B_{sp}/t_{sp}) and the welding length between the side plate and internal short beam flange (l_s). The geometry and the sectional dimensions of the specimens are shown in Fig. 3. The rectangular steel tube of mono-column was 150 × 150 × 6 × 6 mm in size. Meanwhile, the beams were H-shaped steel sections of a cross-section 300 × 150 × 6 × 8 mm for all test specimens. The L-CFST columns and the steel beam were prefabricated in factories. At the test site, the beam flange was welded with a beam flange connecting plate, whereas the beam web and shear plate were connected with high-strength bolts.

Table 1 Summary of the test specimens

Joint type	Specimen	$B_{sp}\times t_{sp}$ (mm× mm)	l_s (mm)	Concrete	n_0
Corner Joint	CJ-H300-1	100×6	40	Hollow	0.28
	CJ-H300-2	75×8	0	Filled	0.28
	CJ-H300-3	100×6	0	Filled	0.28
Exterior Joint	EJ-H300-1	100×6	150	Filled	0.28
	EJ-H300-2	75×8	150	Filled	0.28
Interior Joint	IJ-H300-1	100×6	40	Filled	0.28
	IJ-H300-2	100×6	40	Filled	0.14

*n_0 = the axial compression ratio, $=N/(f_{ymc}A_{mc} + f_cA_c + f_{yvsp}A_{vsp})$, where f_{ymc} = the yield strength of steel tube, f_c = the concrete compressive strength, f_{yvsp} = the yield strength of the vertical steel plate, A_{mc} = the total area of the steel tubes, A_c = the total area of concrete, A_{vsp} = the total area of the vertical steel plates. (Xiong *et al*. 2017)

2.2 Material properties

The standard tensile test results for the steel properties are listed in Table 2, where f_y is the yield strength, f_u is the two 1000-kN tensile-compressive jacks (stroke of ±350 mm).

At the start of loading, a constant axial pressure was applied at the centroid point of the L-CFST columns via

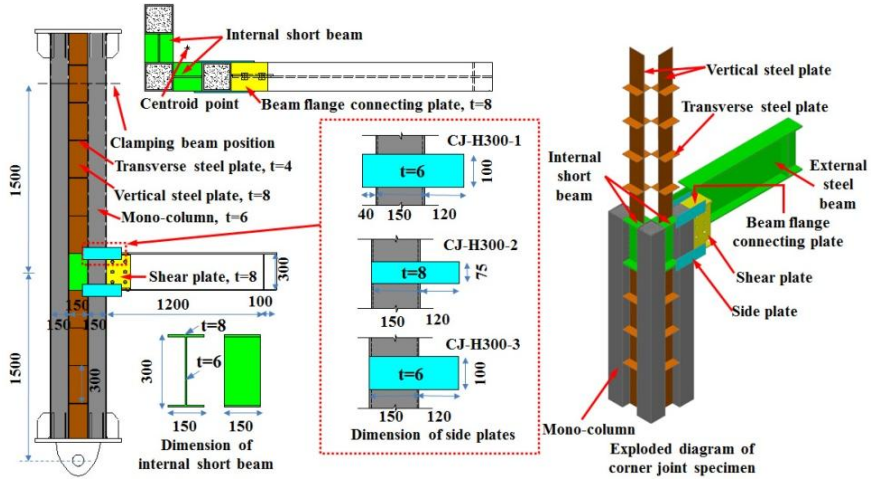

(a) Corner joint specimens

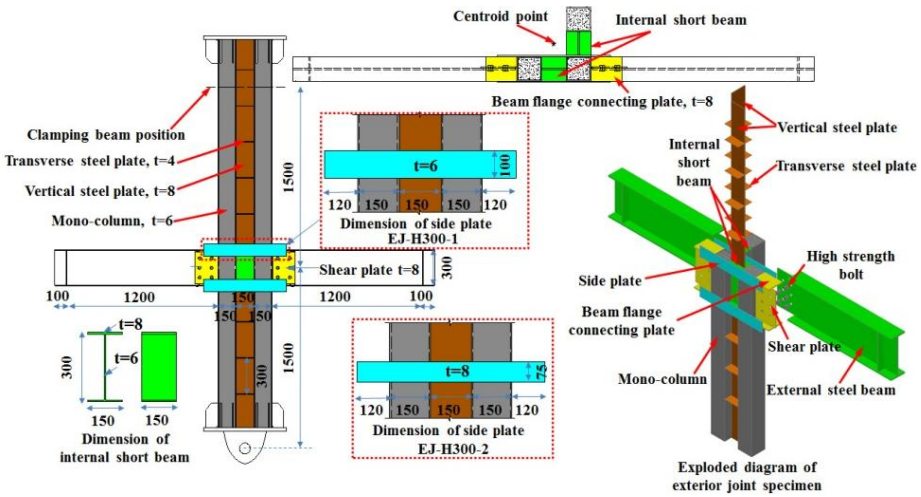

(b) Exterior joint specimens

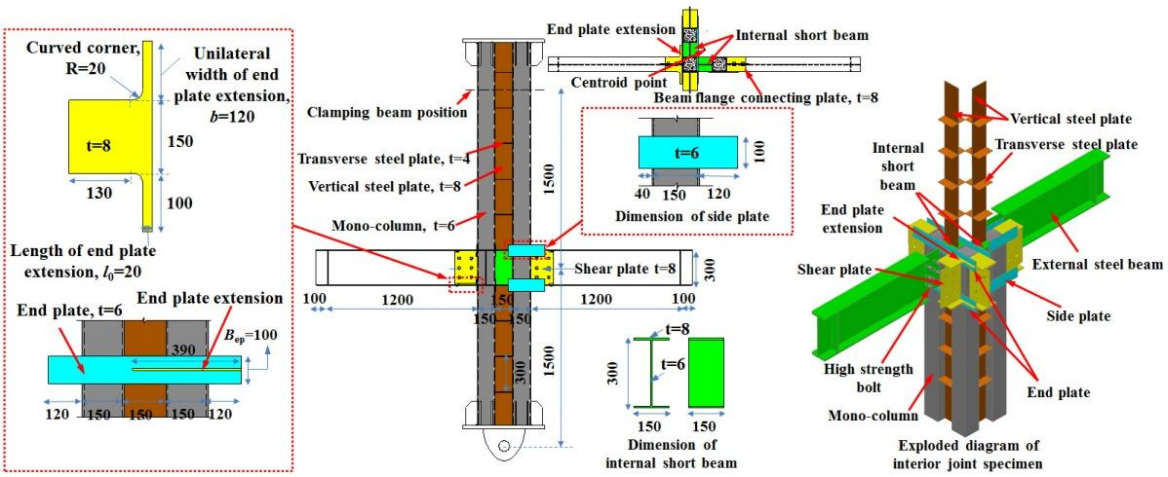

(c) Interior joint specimens

Fig. 3 Geometry of the specimens

several grades. Subsequently, vertical cyclic loading was applied at the beam end. The cyclic loading system at the beam end was referenced to the related test standard (JGJ101-96 1997), as shown in Fig. 5. The force-displacement mixed controlled loading process was divided into two stages. The force control was applied using three grades ($1/3P_y$ kN, $2/3P_y$ kN and P_y kN) prior to material yield, and each grade was repeated once. The displacement control was applied after material yield, and each grade was repeated twice.

Table 2 Experimental results for the material properties

Component	f_y (N/mm^2)	f_u (N/mm^2)	E (10^5 N/mm^2)
Internal short beam flange	381.2	524.5	1.76
Internal short beam web	362.7	501.9	1.95
External steel beam flange	381.2	524.5	1.76
External steel beam web	362.7	501.9	1.95
Side plate ($6 \times 100 \times 310$ mm^3)	362.7	501.9	1.95
Side plate ($8 \times 75 \times 310$ mm^3)	381.2	524.5	1.76
Vertical steel plate	362.7	501.9	1.95
Transverse steel plate	393.6	537.1	1.92
Steel tube	280.3	446.2	1.69

2.4 Instrumentation

The layouts of the displacement transducers are shown in Figs. 6(a) and (b). The cross-arranged dial gauges (D1 and D2) were displayed diagonally in the panel zone of the L-CFST column to calculate the shear distortion. The cross-arranged dial gauges (D3 and D4) were also displayed diagonally in the panel zone of the mono-column. The displacement transducers (D5 and D6) were set at the top and bottom of the L-CFST column to calculate the integral rigid rotation. The displacement transducers (D7 and D8) were placed at the loading points to measure the beam-end displacement. The rotation of the steel beam was measured by inclinometer R1 or R2, and the rotation of the mono-column directly connected to the steel beams was measured by inclinometer R3 or R4. The strain gages were located on steel beam flanges, side plates and transverse steel plates, as shown in Figs. 6(c)-(e).

3. Test results

3.1 Corner joint specimen

Three corner joint specimens failed in a similar fashion, i.e., failure began with micro-cracks within the beam flange connecting plate adjacent to the end of side plates. Specimen CJ-H300-1 displayed a micro-crack at the story drift angle of 0.008 rad; however, the story drift angle of Specimens CJ-H300-2 and CJ-H300-3, the steel tubes of which were infilled concrete, increased approximately 0.008 rad when the micro-cracks began to appear. As the loading increased, the cracks on the beam flange connecting plate extended further, and slight buckling also occurred. The cracks were antisymmetric, i.e., the cracks occurred at

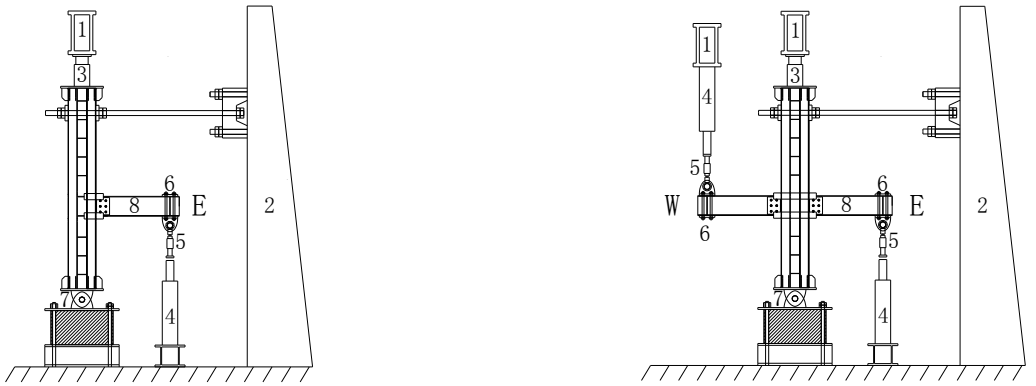

(a) Setup of the corner joint specimens (b) Setup of the exterior and interior joint specimens

Fig. 4 Test setup

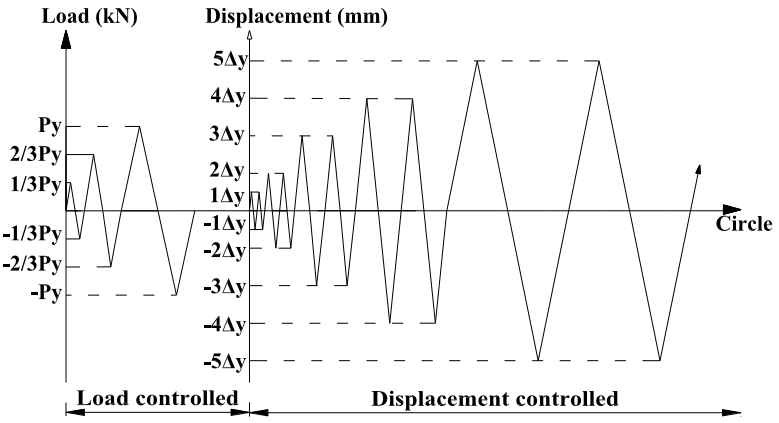

Fig. 5 Loading history

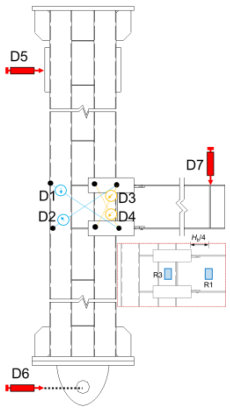

(a) Displacement transducers arranged in corner joint specimens

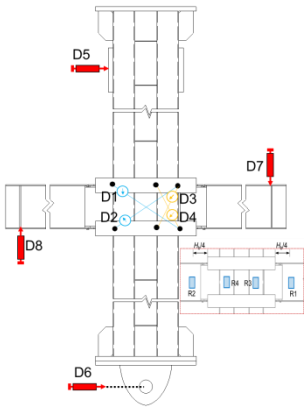

(b) Displacement transducers arranged in exterior and interior joint specimens

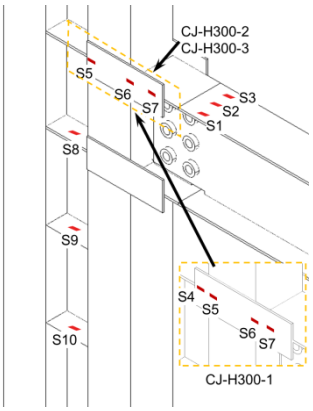

(c) Strain gauges arranged in corner joint specimens

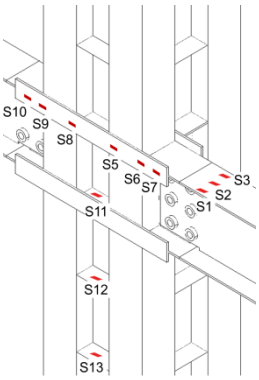

(d) Strain gauges arranged in exterior joint specimens

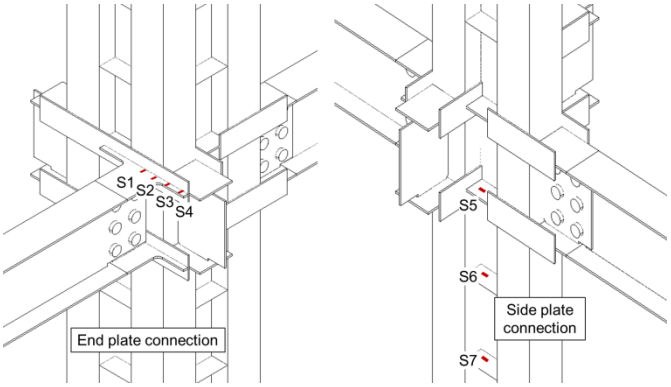

(e) Strain gauges arranged in interior joint specimens

Fig. 6 Arrangement of displacement transducers and strain gauges

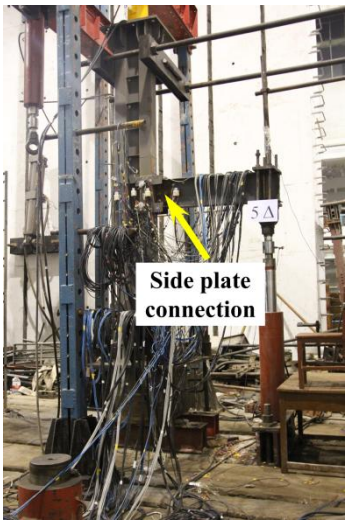

(a)

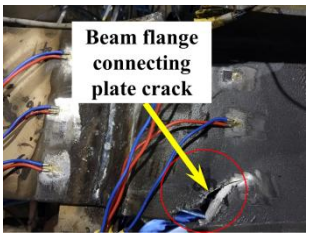

(b)

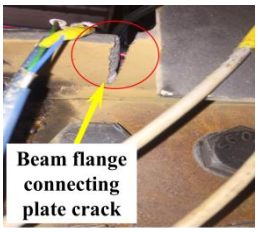

(c)

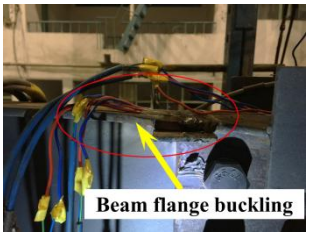

(d)

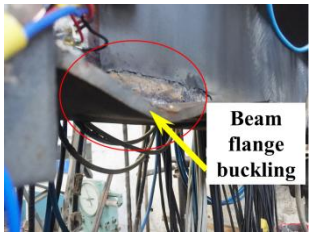

(e)

Fig. 7 Failure modes of the corner joint specimens

the north side of the upper beam flange connecting plate and the south side of the lower beam flange connecting plate. Slight heaves at the column flange were observed by touch, but no obvious deformation or cracks were observed in the panel zone. Finally, as the cracks extended to the shear plate, the steel beam became seriously twisted, and the force dropped to 85% of the peak force. The effect on the failure modes of the welding length between the side plate and the internal short beam flange can be ignored throughout the loading process. No crack was observed at

the weld between the vertical steel plate and the mono-column in the L-CFST columns. The final failure modes of the corner joint specimens are presented in Fig. 7. In addition, this ductile tearing near the end of side plates is common practical problem which has been reported by Ghobadi *et al*. (2009b), and Mehr and Ghobadi (2017).

The primary reasons for the cracks that appeared in the beam flange connecting plate are the following:

(1) The stress concentration caused by sudden changes in the beam sections at the end of the side plate cannot be ignored;
(2) The weakness of heat affected zone (HAZ) of base metal at the weld position intensified the cracks;
(3) The column section was L-shaped; therefore, the transverse force at the column did not pass through the shear centre of the section. The L-CFST columns thus exhibited slight torsion and shear effects at the ends of the side plates, which intensified the cracks in the beam flange connecting plate.

3.2 Exterior joint specimen

The only difference between the two exterior joint specimens was the width-to-thickness ratio of the side plates. Additionally, the exterior joint specimens both displayed cracks at the beam flange connecting plate, similar to those of the corner joint specimens; however, the story drift angle corresponding to the first appearance of the micro crack in the two exterior joint specimens was different. When the cracks appeared in Specimen EJ-H300-2 with a smaller width-to-thickness ratio of the side plate, the story drift angle was 0.022 rad, which was greater than that of Specimen EJ-H300-1 with a greater width-to-thickness ratio. This result illustrated that the width-to-thickness ratio of the side plate had some effect on the cracks; however, the influence was not obvious in the corner joint specimens. The primary reason for this result was that the symmetric loading of the exterior joint specimens limited the torsion of the L-CFST column; hence, the risk of cracking caused by the torsion of the L-CFST column was reduced. The influence of the width-to-thickness ratio of the side plates was thus the major cause for the crack of the beam flange connecting plate. As loading continued, the antisymmetric cracks on the beam flange connecting plate were further extended, and slight buckling of the beam flange also occurred. Finally, as the cracks in Specimen EJ-H300-1 extended to the shear plate, the steel beam was severely twisted, and the beam-end force was reduced to 85% of the peak force. However, during the 5Δy negative loading process, a distinctive sound was emitted from Specimen EJ-H300-2.The lower flange weld seam of the east beam cracked. This crack was accompanied by a sharp reduction in the beam-end force and dramatic growth in the displacement. The final failure modes of the exterior joint specimens are presented in Fig. 8.

3.3 Interior joint specimen

In the interior joint Specimens IJ-H300-1 and IJ-H300-2, the end plate connection was placed between the left steel beam and the central mono-column, and the side plate connection was placed between the right steel beam and the side mono-column. The only difference between the two interior specimens was the axial compression ratio. As loading progressed, the failure phenomena of the interior joint specimens occurred primarily at the end plate connection. Initially, micro cracks were generated at the weld position of the end plate. Subsequently, crack and buckling developed at the curved corners. The beam flange pulled the end plate tearing, and the heave on the end plate intensified as the loading continued. Simultaneously, the beam-end force declined dramatically. During the entire loading process, the side plate connection exhibited only slight crack at the ends of the side plates. Comparing the failure phenomena of two specimens, as the axial

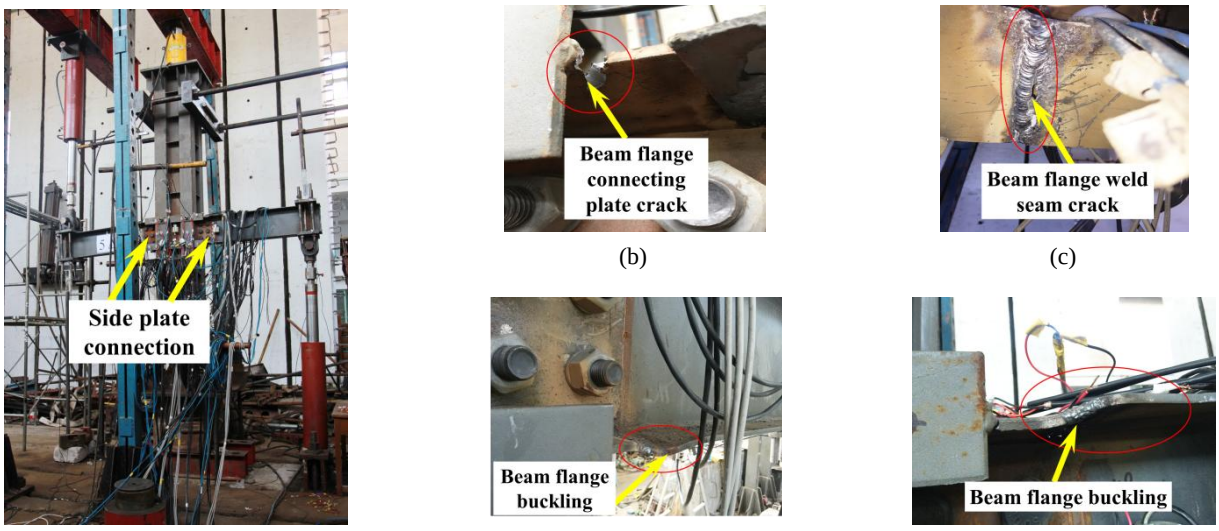

Fig. 8 Failure modes of the exterior joint specimens

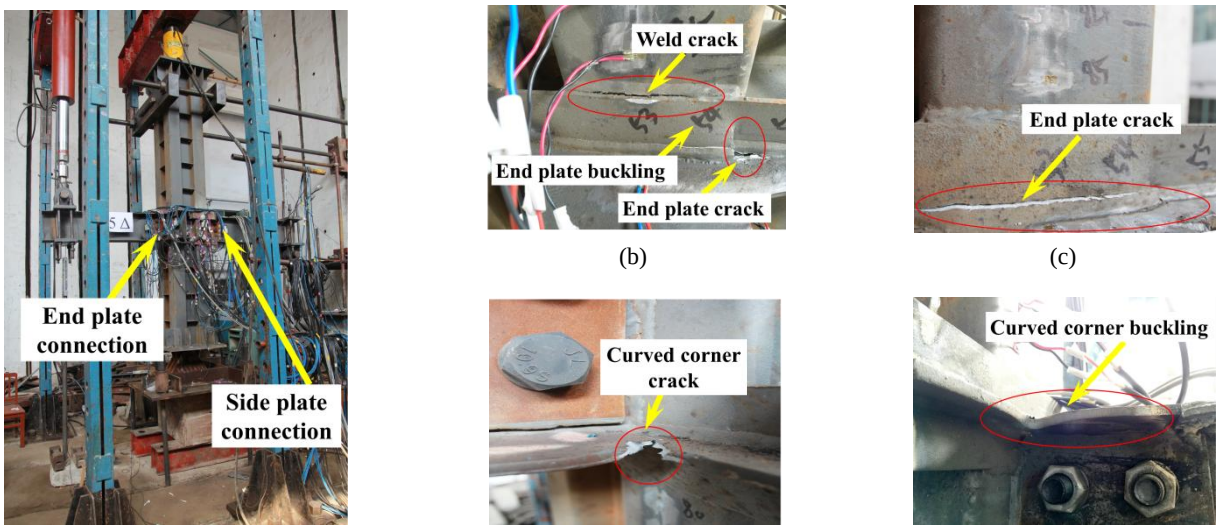

(a) (b) (c) (d) (e)

Fig. 9 Failure models of the interior joint specimens

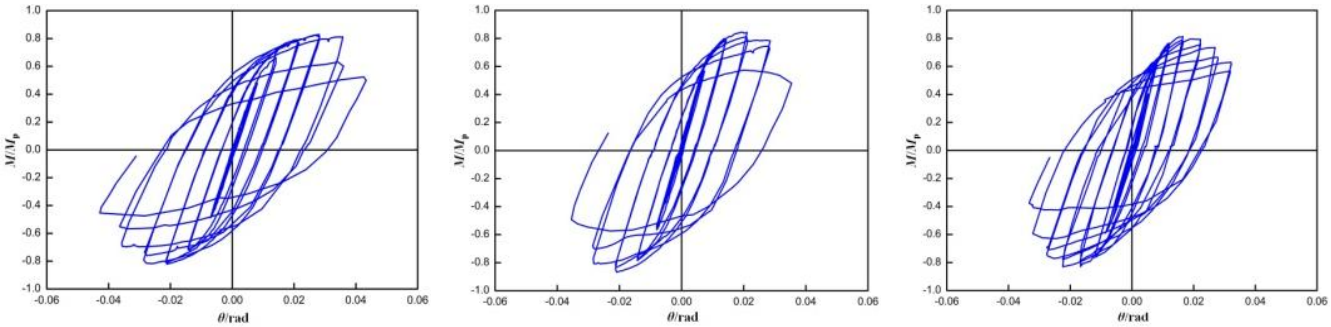

(a) Specimen CJ-H300-1 (b) Specimen CJ-H300-2 (c) Specimen CJ-H300-3

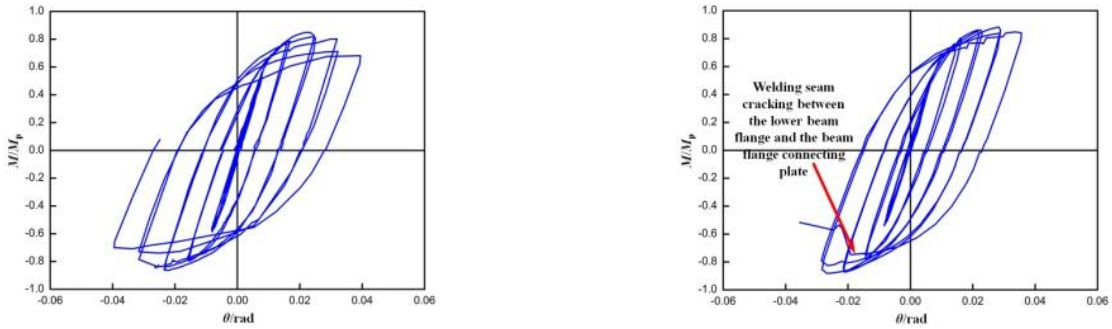

(d) Specimen EJ-H300-1 (e) Specimen EJ-H300-2

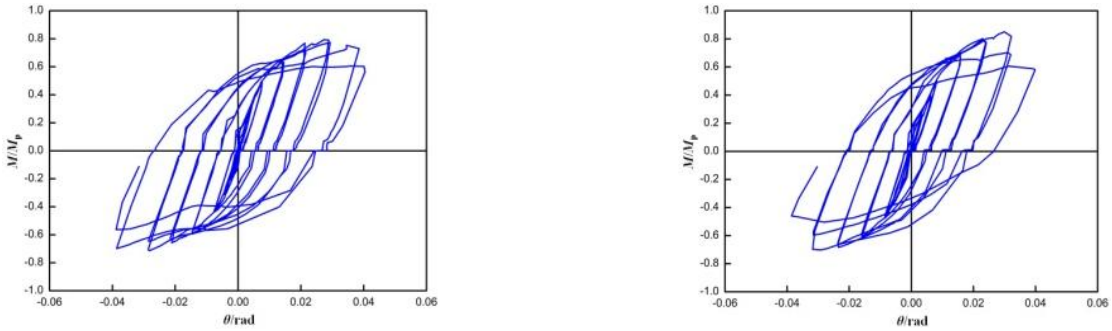

(f) Specimen IJ-H300-1 (g) Specimen IJ-H300-2

Fig. 10 Specimens' hysteresis responses of normalized moment - story drift angle

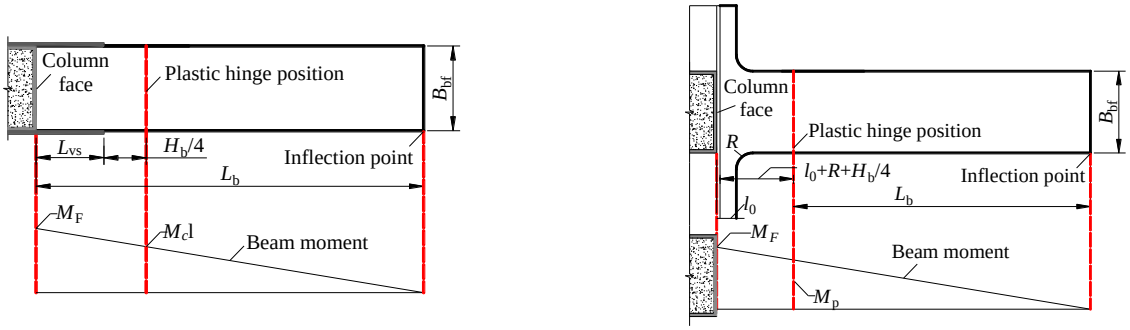

(a) Corner and exterior joint (b) Interior joint

Fig. 11 Calculation method diagram of the moment at the plastic hinge location

compression ratio increased, the degree of failure increased. With a higher axial compression ratio, Specimen IJ-H300-1 exhibited wide vertical cracks in the end plate and a cracked fillet weld between the end plate and the steel tube, which also destroyed the steel tube wall. The final failure modes of the interior joint specimens are presented in Fig. 9.

4. Analysis and discussion

4.1 Moment-rotation response

The moment-rotation response is a key element used to evaluate the performance of the beam-to-column connections. The M/M_p-θ hysteresis curves for seven specimens are shown in Fig. 10. Here, M is the moment of the plastic hinge location as shown in Fig. 11. In addition, M_p is the plastic moment of beam full section, and θ is the story drift angle, which can be regarded as the ratio of the displacement at the beam-end application loading position to the distance from the beam-end application loading position to the centroid of the nearest mono-column (Ma *et al*. 2017). The hysteresis loops of all specimens were plump with little noticeable pinching effect. When the moment was small, the hysteresis loop was generally linear, indicating that the specimens were in an elastic stage. The hysteresis loop of this stage had a minimal surrounding area. The residual deformation after unloading was small, and no significant degradation in stiffness was noted. During the displacement control stage, the hysteresis loop area increased as the story drift angle increased. The hysteresis loop gradually tilted to the story drift angle axis, and the stiffness of the joint specimens decreased. For the corner and exterior joint specimens, these phenomena occur from the development of cracks and the buckling of the beam flange. For the interior joint specimens, these phenomena occur from the cracks and buckling at the end plates and the curved corners.

As presented by Shin *et al*. (2004), the concept of the envelope curve has been widely adopted in Japan for the characterization of the deformation of structural members subjected to reversal loads. The envelope curves are compared in Fig. 12. The moment of plastic hinge position (M) and story drift angle (θ)) obtained are summarized in Table 3. The ratio of the peak moment at plastic hinge position to the plastic moment of beam full section is also listed in Table 3.

In general, specimens with the same connections exhibited a similar moment versus story drift angle responses.

(1) Different types of joints displayed significantly different bearing capacity, ductility and stiffness. Based on a comparison of Specimens CJ-H300-3, EJ-H300-1 and IJ-H300-1, corner joint specimens with asymmetric loading conditions had a lower peak moment and a sharper moment reduction after the peak point compared with exterior joint specimens. Additionally, the L-CFST columns produced horizontal shear and torque during the loading process. Synchronous loading at two sides of the exterior joint specimens relieved the shear force and torque at the beam ends, thus resulting in a low cracking degree and strong ductility of the beam flange connecting plates. The stiffness and the peak bearing capacity of the interior joint specimens were significantly reduced compared with the exterior and corner joint specimens.

(2) The bearing capacity and ductility of the specimens were influenced by the width-to-thickness ratio of the side plate. The results from the comparison between Specimens EJ-H300-1 and EJ-H300-2 demonstrated that as the width-to-thickness ratio of the side plate decreased, the peak bearing capacity and ductility increased.

(3) The infilled concrete influenced the peak bearing

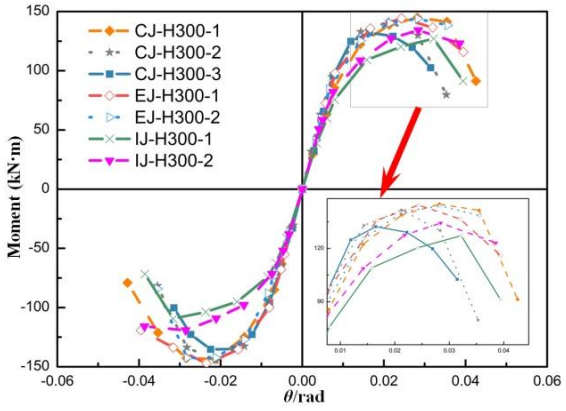

Fig. 12 Envelope curves

Table 3 Summary of test results

Specimen & Loading Direction		θ_y (rad)	M_y (kN·m)	θ_m (mm)	M_m (kN)	θ_u (mm)	M_u (kN)	M_m/M_p	The reasons for test termination and failure modes
CJ-H300-1	+	0.013	109.38	0.028	138.68	0.038	117.88	0.84	* $M \le 0.85 \cdot M_m$ * Failure modes A and B
	-	-0.010	-99.99	-0.028	-137.43	-0.035	-116.82	-0.83	
CJ-H300-2	+	0.009	101.76	0.021	135.47	0.030	115.15	0.82	
	-	-0.010	-105.18	-0.021	-138.19	-0.030	-117.44	-0.83	
CJ-H300-3	+	0.009	103.69	0.022	126.56	0.029	107.58	0.76	
	-	-0.009	-99.79	-0.022	-129.41	-0.029	-110.01	-0.78	
EJ-H300-1	+	0.011	105.99	0.024	138.15	0.037	117.42	0.83	
	-	-0.011	-108.35	-0.023	-140.81	-0.036	-119.69	-0.85	
EJ-H300-2	+	0.011	106.07	0.028	137.79	0.036	119.45	0.84	* Beam flange weld cracked * $M \le 0.85 \cdot M_m$ * Failure modes A and B
	-	-0.010	-106.14	-0.028	-136.36	-0.036	-118.21	-0.85	
IJ-H300-1	+	0.013	97.06	0.028	133.25	0.036	105.54	0.80	* $M \le 0.85 \cdot M_m$ * Failure modes C, D and E
	-	-0.012	-82.67	-0.029	-114.51	-0.035	-90.70	-0.70	
IJ-H300-2	+	0.013	109.38	0.028	140.66	0.038	117.88	0.85	
	-	-0.010	-99.99	-0.028	-124.86	-0.035	-116.82	-0.75	

*Failure modes of specimens
A: the crack at beam flange connecting plate; B: the buckling at beam flange; C: the crack at end plate; D: the crack at curved corner of end plate extension; E: the buckling at curved corner of end plate extension

stiffness and ductility. Given that cracks and local buckling of the beam flange were the main failure modes of the corner and exterior joint specimens, the infilled concrete had a small influence on the peak bearing capacity. However, the infilled concrete restricted the depressed deformation of the column wall in the panel zone and decreased the story drift angle of joints under the yield force, thus increasing the ductility factor of the joints in a relative manner.

(4) The axial compression ratio influenced the bearing capacity and ductility. According to a comparison of Specimens IJ-H300-1 and IJ-H300-2, the bearing capacity and ductility of the interior joint specimen decreased slightly as the axial compression ratio increased.

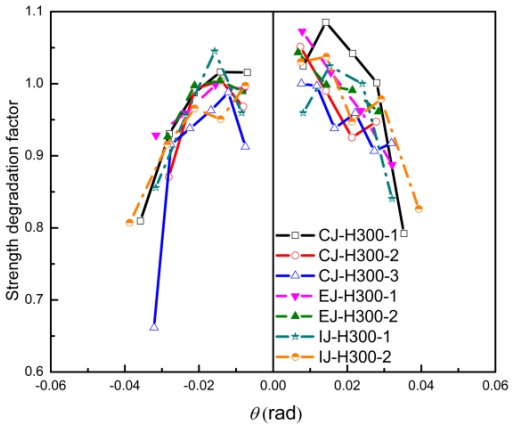

Fig. 13 Strength degradation of the specimens

4.2 Strength degradation

As the principal approach to evaluating the performance of beam-to-column connections under cyclic loading, strength degradation is defined as the loss of strength with cyclic loading. Strength degradation is evaluated using the strength degradation factor (η_j), which is defined as the ratio of the maximum strength in the last cycle to that in the first cycle at the same displacement level, as provided in Eq. (1)

$$\eta_j = \frac{M_j^n}{M_j^i} \tag{1}$$

where n = the number of cycles at the displacement level of j and M_j^i = the maximum strength of the ith cycle at the displacement level of j.

The values of η_j at different displacement levels for all specimens are plotted in Fig. 13. The data demonstrate that η_j gradually decreased as the story drift angle increased. The strength degradation increased as the cycles progressed. Before the peak point, η_j generally ranged from 0.95 to 1.07, indicating moderate strength deterioration prior to peak capacity. After the peak point, the strength degradation was more severe, as evidenced by the data. The primary cause of the strength degradation was that the cracks on the beam flange connecting plate of the corner and exterior joint specimens further accelerated and intensified, whereas the interior joint specimens experienced buckling and

cracks at the end plate and curved corner after reaching the peak bearing capacity. The bearing capacity of all specimens at the fracture point was greater than 0.8, except for Specimen CJ-H300-3. The strength degradation of the exterior joint specimens was less than that of the corner joint specimens. This result may be attributed to the fact that because the symmetric loading condition relieved the stress concentration and the tear fracture on the beam flange.

4.3 Stiffness degradation

The stiffness degradation factor (ξ_j) (Applied Technology Council 2009) can be defined as the ratio of the average secant stiffness at the displacement level of j (K_j) to the initial stiffness (K_0), as shown in Eq. (2) as follows

$$\xi_j = \frac{K_j}{K_0} \tag{2}$$

where the averaged secant stiffness (K_j) is defined as the ratio of the sum of the secant stiffness at the displacement level of j ($\sum_{i=1}^{n} K_j^i$) to the number of cycles (n) at displacement level of j. This relationship is shown in Eq. (3) as follows

$$K_j = \frac{\sum_{i=1}^{n} K_j^i}{n} \tag{3}$$

The secant stiffness K_j^i is then determined by Eq. (4), where U_j^i is the recorded beam end displacement of the ith cycle at the displacement level of j and F_j^i is the recorded beam-end load of the ith cycle at the displacement level of j as follows

$$K_j^i = \frac{\left|+M_j^i\right| + \left|-M_j^i\right|}{\left|+\theta_j^i\right| + \left|-\theta_j^i\right|} \tag{4}$$

Figs. 14 and 15 present plots of the K_j-θ curves and the ξ-θ curves, respectively, for the seven specimens. The cyclic stiffness degradation responses were compared, and the following results were obtained:

(1) The stiffness degradation of the seven specimens had a similar tendency to decrease. Stiffness and stiffness degradation were significantly influenced by the infilled concrete. Specimen CJ-H300-3 with infilled concrete had a large initial stiffness compared with Specimen CJ-H300-1. However, the stiffness degradation of Specimen CJ-H300-3 was increased compared with Specimen CJ-H300-1.
(2) The data revealed differences among specimens with different axial compression ratios. The initial secant stiffness of Specimen IJ-H300-1 was increase compared with that of Specimen IJ-H300-2. However, the stiffness degradation rate was generally the same.
(3) Initial stiffness and stiffness degradation were greatly affected by the joint type. The exterior and corner joint specimens generally had the same initial stiffness, but the stiffness degradation of the corner joint specimens was more rapid. Given the effect of the end plate connection to the left beam, the interior joint specimens exhibited reduced initial stiffness and stiffness degradation compared with the exterior and corner joint specimens.

4.4 Ductility, plastic rotation capacity and energy dissipation capacity

Ductility is defined as the ability of the structure to undergo a large plastic deformation without noticeable strength degradation. To assess the ductility of the specimens, the ductility factor (μ) is calculated using Eq. (5) as follows

$$\mu = \frac{\theta_u}{\theta_y} \tag{5}$$

where θ_y is the story drift angle related to the yield strength, and θ_u is typically the story drift angle corresponding to the designed ultimate strength, which is equal to $0.85M_m$. The ductility factor for each specimens is presented in Table 4. The ductility factors range between 2.86 and 3.39. The welding effect, the stress concentration caused by side plates, and the shearing force and torque produced by the L-

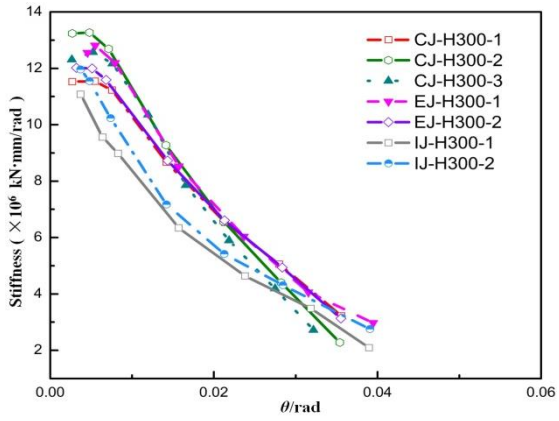

Fig. 14 Curves of stiffness versus story drift angle

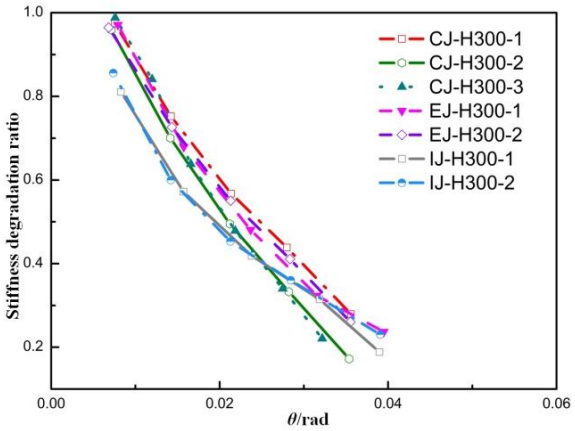

Fig. 15 Curves of the stiffness degradation ratio versus story drift angle

Table 4 Ductility, plastic rotation capacity and energy dissipation capacity

Specimen		Corner joint			Exterior joint		Interior joint	
		CJ-H300-1	CJ-H300-2	CJ-H300-3	EJ-H300-1	EJ-H300-2	IJ-H300-1	IJ-H300-2
μ	+	2.98	3.17	3.07	3.36	3.31	2.86	3.21
	-	2.93	3.06	3.08	3.32	3.47	2.86	3.13
$\bar{\mu}$		2.96	3.12	3.08	3.34	3.39	2.86	3.17
θ_p (rad)		0.020	0.023	0.022	0.024	0.024	0.027	0.028
h_e	$1\Delta_y$	0.037	0.032	0.039	0.041	0.034	0.076	0.094
	$2\Delta_y$	0.141	0.145	0.111	0.178	0.148	0.184	0.195
	$3\Delta_y$	0.221	0.22	0.219	0.274	0.223	0.255	0.256
	$4\Delta_y$	0.284	0.327	0.258	0.33	0.293	0.294	0.301
	$5\Delta_y$	0.301	0.447	0.32	0.347	0.356	0.337	0.331
	$6\Delta_y$	-	-	0.352	-	-	-	-

CFST columns, which intensified the brittle fracture of the beam flange, influenced the ductility development.

The plastic rotation capacity of the connections can be calculated using Eq. (6) as follows

$$\theta_p = \theta_b - \theta_{mc} \tag{6}$$

where θ_b = the rotation of the steel beam measured by the inclinometers R1 and R2; and θ_{mc} = the rotation of the mono-columns directly connected to steel beams. These rotations were measured by inclinometers R3 and R4.

The ultimate plastic rotations of all the specimens (Table 4) were between 0.02 and 0.03. The data in Table 3 demonstrate that the ratios of the peak flexural strengths and plastic moments of the full section were generally equal to 0.8. Therefore, according to AISC341-05 (2005), the L-CFST column frame system composed of such connections belongs to the intermediate moment frame (IMF). However, high-rise steel structure residential buildings with the L-CFST column structural system typically adopt braces, shear walls or reinforced concrete cores to resist most of the lateral load, and the L-CFST column moment frame is required to resist only a small portion of the lateral load. Therefore, the connections can also be used in high-rise steel structure residential buildings.

The energy dissipation capacity of the connections is one of the most important factors in their seismic performance (Chopra 2005, Fardis and Panagiotakos 1997). The energy absorbed by the deformation of the specimen can be measured using the areas enclosed by the moment-rotation hysteresis loop, as illustrated in Fig. 16. The equivalent damping coefficient h_e is calculated using Eq. (7) as follows

$$h_e = \frac{S_{(ABC+CDA)}}{2\pi S_{(OBE+ODF)}} \tag{7}$$

where $S_{(ABC+CDA)}$ = area enclosed by the hysteresis loop and $S_{(OBE+ODF)}$ = summation of the triangular areas OBE and ODF. The calculated values for h_e are presented in Table 4.

As expected, the energy dissipation capacity of the specimens stably increased as the load amplitude of the

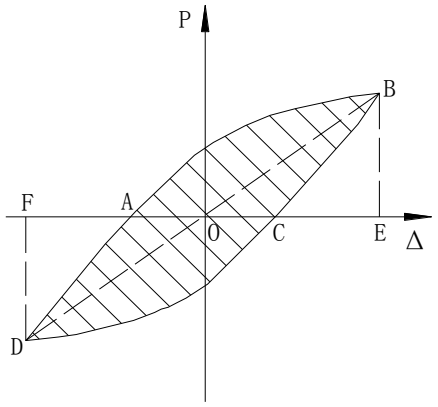

Fig. 16 Equivalent damping coefficient calculation diagram

hysteresis loops increased, up to the failure point. At the ultimate point, the maximum and minimum equivalent damping coefficients are 0.447 and 0.301, respectively. Additionally, the data in Fig. 17 demonstrate that the crack and buckling within the beam flange, and the heave and crack within the end plate and curved corner were the manifestations of full plasticity development and increasing energy consumption capacity. In summary, the connections between the L-CFST columns and steel beams exhibited better energy consumption capacity than other flange-strengthened connections (Ma *et al*. 2017).

4.5 Strain distribution

Strains in the regions of the beam flanges, side plates and transverse steel plates were analysed. Particular attention was focused on the strain status corresponding to the last cycle of the different loading displacement grades. For ease of presentation, the strain distributions of CJ-H300-3, EJ-H300-1 and IJ-H300-2 are used to represent their groups for the following discussion.

The distribution of the strains in the beam flange along the transverse direction is presented in Figs. 18(a)-(c), where Δy is the identified yield beam-end displacement joint specimens, the strain distributions at three measurement points on the beam flange were generally

during the test loading process. For corner and exterior consistent early in the loading process. The maximum strain of the beam flange exceeded the yield strain late in the loading process, but the plasticity did not completely develop. The strain developments at three measurement points on the beam flange were significantly different. The tensile strains on the S1 measurement point changed to compressive strains late in the loading process, and most were close to or exceeded the yield compressive strain, which was caused by the torque of the steel beam after the crack of the top north beam flange. The strain distributions were consistent with the characteristics reflected by the test phenomena and load-displacement curves. For the interior joint specimen, the S2 measurement point had the largest strain, whereas the S3 and S4 measurement points, which were located far away from the beam flange centre, had significantly lower strains (close to 0).

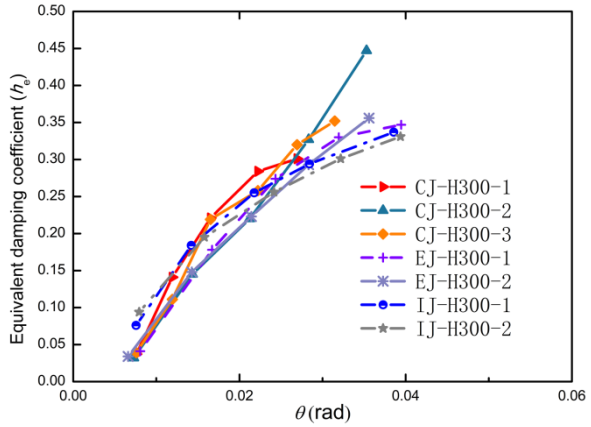

Fig. 17 Equivalent damping coefficient

The data in Figs. 18(d)-(f) demonstrate the response of the strains in the side plate along the horizontal direction. Except for Specimen CJ-H300-1 without infilled concrete, the strains of the other specimens under the tension of the side plate were within the yield strains. The maximum tensile strain occurred at the interface between the side plate and the column flange, i.e., the positions of the S6 and S9

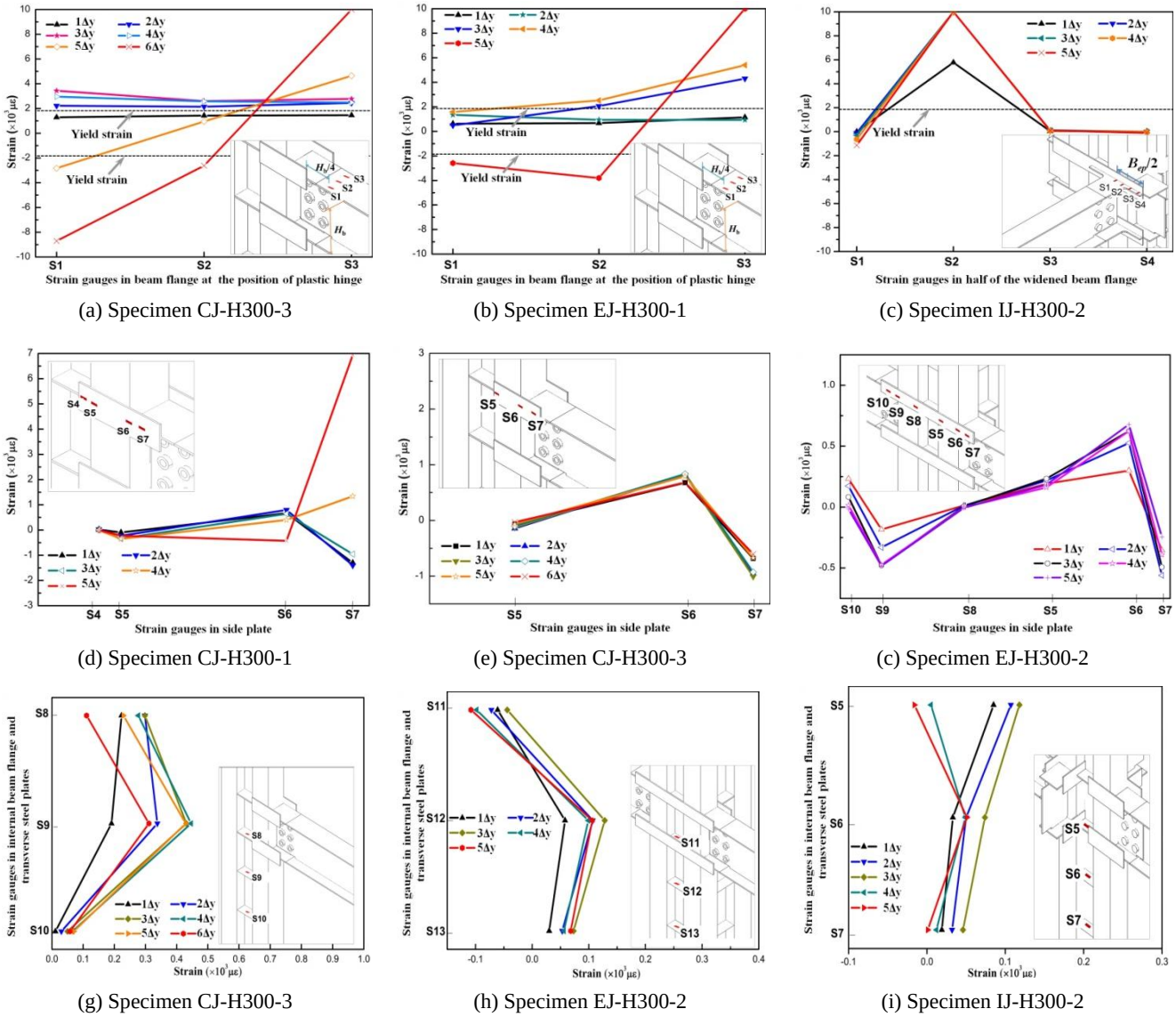

(a) Specimen CJ-H300-3 (b) Specimen EJ-H300-1 (c) Specimen IJ-H300-2

(d) Specimen CJ-H300-1 (e) Specimen CJ-H300-3 (c) Specimen EJ-H300-2

(g) Specimen CJ-H300-3 (h) Specimen EJ-H300-2 (i) Specimen IJ-H300-2

Fig. 18 Strain distribution in critical positions of the specimens at the last cycle of loading

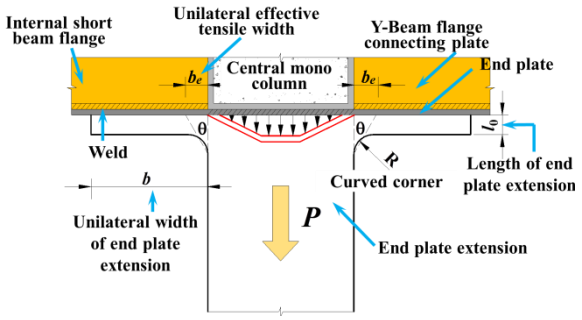

Fig. 19 Deformation of the end plate

strain gauges. Strains decreased from the outside to the inside. The strain distribution law and strain values remained the same when the 40 mm length of side plate welded to the internal beam flange was eliminated.

The distributions of the strains in the internal short beam bottom flange and within 600 mm of the transverse steel plates along the longitudinal direction distance from the panel zone are presented in Figs. 18(g)-(i). The vertical axes represent the numbers of the strain gauges at three relative positions. The data indicate that the horizontal tensile strains of the transverse steel plates were negatively correlated with the distance from the panel zone. As the distance from the panel zone increased, the tensile strain of the transverse steel plate decreased. These results demonstrate that setting the transverse steel plates within 600 mm of the panel zone in L-CFST columns satisfies the requirements.

5. Flexural capacity of end-plate connection in interior joint

The test results revealed that the stiffness and strength of the end plate connections were weaker compared with those of the side plate connections in the same plane. Therefore, it is necessary to propose a calculation method of the flexural capacity of the end plate connections. The out-of-plane deformation of the end plate, which is caused by the tension of the steel beam flange, is illustrated in Fig. 19.

For the end plate connection in interior joint, the steel beam flange was connected by the end plate to the mono-column flange. According to the calculation method of the flexural capacity of the internal- and through- diaphragm connection (Nie *et al*. 2009, Qin *et al*. 2014), the end plate can be regarded as a "beam flange with a large thickness", which causes the buckling deformation of the column flange. However, the end plate is different from the ordinary steel beam flange, and its width-to-thickness ratio is large which resulting in the occurrence of buckling deformation. Therefore, in the use of the theory of yield-line mechanism, the contribution of the steel tube and end plate should be considered. At the same time, the end plate extension will transfer part of force to the weld between the internal/external beam flange and the end plate. The contribution of the weld to the flexural capacity should also not be ignored. The calculation of the yield flexural capacity of the end plate connection in the interior joint is shown in Eq. (8) as follows

$$M_{PY} = \left(P_{epy} + P_{mcfy} + P_w\right) \cdot (H_b - t_{bf}) \tag{8}$$

where M_{PY} = the yield flexural capacity of the end plate connection, P_{epy} = the yield tensile capacity of the end plate; P_{mcfy} = the yield tensile capacity of the mono-column flange, P_w = the tensile capacity of two-side weld outside of the mono-column flange, H_b = the height of the steel beam, and t_{bf} = thickness of steel beam flange.

The yield tensile capacity of end plate (P_{epy}) can be calculated using the yield-line theory, which has been used by many scholars and its correctness has been verified (Jazany and Ghobadi 2017, Jafarian and Wang 2015, Nie *et al*. 2009). The calculation method of P_{epy} is shown in Fig. 20 and Eq. (9).

For the yield-line model of the end plate, the maximum vertical length of the yield line is the width of the end plate, while the transverse length of the yield line near the beam flange connecting plate is assumed to be X. Therefore, the yield lines on the end plate are numbered 1 to 8. According to the principle of virtual work, the tensile force of the end plate can be obtained as

$$P_{epy} = m_{ay}\left(\frac{4\left(B_{mc}+X\right)}{B_{ep}-t_{bf}} + \frac{4\left(B_{ep}-t_{bf}\right)}{B_{mc}-X}\right) + m_{by}\frac{4B_{mc}}{B_{ep}-t_{bf}} \tag{9}$$

$$m_{ay} = \frac{1}{4} f_{epy} t_{ep}^2 \tag{10}$$

$$m_{by} = \min\left\{\frac{1}{4} f_{epy} t_{ep}^2, \frac{1}{4} f_w t_{ep}^2, \frac{1}{4} f_{mcy} t_{mc}^2\right\} \tag{11}$$

where m_{ay} = the yield moment of unit length in end plate; m_{by} = the yield moment of unit length at the position of weld between end plate and steel tube; f_{epy} = the yield strength of end plate; f_w = the strength of weld between end plate and steel tube; f_{mcy} = the yield strength of steel tube;

X can be determined by the condition where the solution P_{epy} is minimized, i.e.

$$\frac{\partial P_{epy}}{\partial X} = m_{ay}\left(\frac{4}{B_{ep}-t_{bf}} + \frac{4\left(B_{ep}-t_{bf}\right)}{\left(B_{mc}-X\right)^2}\right) > 0 \tag{12}$$

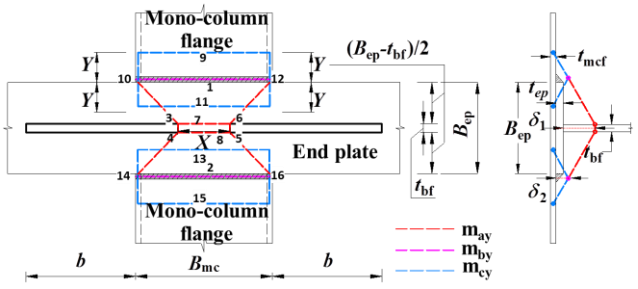

Fig. 20 Yield-line mechanism of end plate under tension force

When $X = 0$, the minimum value of P_{epy} can be obtained. By substituting $X = 0$ into Eq. (9), the tensile capacity of end plate can be calculated as follows

$$P_{\mathrm{epy}} = m_{ay}\left(\frac{4B_{mc}}{B_{ep}-t_{bf}} + \frac{4\left(B_{ep}-t_{bf}\right)}{B_{mc}}\right) + m_{\mathrm{by}}\frac{4B_{mc}}{B_{ep}-t_{bf}} \quad (13)$$

Similarly, the yield tensile capacity of the mono-column flange can be obtained using the same calculation method and the yield lines on the mono-column flange are numbered 9 to 16. The maximum vertical length of the yield line at the mono-column flange is assumed to be Y and its value can be obtained according to the minimum tensile force of the mono-column flange. The yield tensile capacity of the mono-column flange is as follows

$$P_{mcfy} = 2t_{mc}f_{mcy}\sqrt{B_{mc}t_{mc}} + 8B_{mc}m_{cy}\frac{1}{\sqrt{B_{mc}t_{mc}}} \quad (14)$$

$$m_{\mathrm{cy}} = \frac{1}{4}f_{mcy}t_{mc}^2 \quad (15)$$

where P_{mcfy} = the yield tensile capacity of mono-column flange; B_{ep} and t_{ep} = the width and thickness of end plate, respectively; B_{mc} = the width of the mono-column flange; t_{bf} = the thickness of the steel beam flange; m_{cy} = the yield moment of unit length in steel tube; f_{mcy} = the yield strength of steel tube;

For two sides of the end plate outside of the mono-column flange, the calculation method of P_w is shown in Eq. (16)

$$P_w = 4f_{\mathrm{w}}b_e h_e \quad (16)$$

where h_e = the calculated thickness of weld; b_e = unilateral effective tensile width, as shown in Eq. (17) and Fig. 19

$$b_e = \left(l_0 + R\right)\tan\theta \quad (17)$$

where l_0 = length of end plate extension; θ = angle of stress dispersion, equal to 30° (GB50017-2003, 2003);

Previous studies (Nie *et al*. 2009) indicated that the ultimate flexural capacity of the connections can be calculated by using the ultimate strength of steel instead of the yield strength of steel in the formulae proposed above. As a result, both the yield and ultimate flexural capacities of the end connection can be calculated as shown in Eqs. (18) and (19)

$$M_{PY} = \left(\begin{array}{l} m_{ay}\left(\frac{4B_{mc}}{B_{ep}-t_{bf}} + \frac{4\left(B_{ep}-t_{bf}\right)}{B_{mc}}\right) + \\ m_{\mathrm{by}}\frac{4B_{mc}}{B_{ep}-t_{bf}} + \\ 2t_{mc}f_{mcy}\sqrt{B_{mc}t_{mc}} + 8B_{mc}m_{cy}\frac{1}{\sqrt{B_{mc}t_{mc}}} + \\ 4f_{\mathrm{w}}h_e\left(l_0+R\right)\tan\theta \end{array}\right) \times \left(H_b - t_{bf}\right) \quad (18)$$

$$M_{PU} = \left(\begin{array}{l} m_{au}\left(\frac{4B_{mc}}{B_{ep}-t_{bf}} + \frac{4\left(B_{ep}-t_{bf}\right)}{B_{mc}}\right) + \\ m_{\mathrm{bu}}\frac{4B_{mc}}{B_{ep}-t_{bf}} + \\ 2t_{mc}f_{mcu}\sqrt{B_{mc}t_{mc}} + 8B_{mc}m_{cu}\frac{1}{\sqrt{B_{mc}t_{mc}}} + \\ 4f_{\mathrm{w}}h_e\left(l_0+R\right)\tan\theta \end{array}\right) \times \left(H_b - t_{bf}\right) \quad (19)$$

where m_{au}, m_{bu} and m_{cu} = the ultimate moment of unit length in end plate, the ultimate moment of unit length at the position of weld between end plate and steel tube, and the ultimate moment of unit length in steel tube, respectively;

The comparison of the test results and theoretical formulas proposed above for the yield and ultimate flexural capacity of the end plate connections is presented in Table 5. The data in the table indicate that the predicted yield flexural capacity agrees well with the experimental data. In addition, the predicted flexural capacity is relatively conservative and thus safe for engineering application.

6. Conclusions

In this study, cyclic loading tests were conducted on three groups of 7 full-scale specimens, and the test results were discussed. The conclusions are summarized as follows:

- The exterior and corner joint specimens both exhibited local buckling and crack at the beam flange. The bearing capacity, ductility, strength degradation ratio and stiffness degradation ratio of the corner joint specimens were reduced compared with those of the exterior joint specimens. The infilled concrete made a small contribution to the peak bearing capacity but increased the stiffness of the joint significantly. The ductility of the joint also increased after concrete

Table 5 Comparison of the experimental and predictive values for the end plate connections

Specimen	Test average results (kN·m)		Proposed formula (kN·m)		$\frac{M_{PY}}{M_{TY}}$	$\frac{M_{PU}}{M_{TU}}$
	M_{TY}	M_{TP}	M_{PY}	M_{PU}		
IJ-H300-1	109.9	151.5	97.0	135.1	0.882	0.892
IJ-H300-2	128.1	162.4			0.758	0.832
Average	-	-	-	-	0.820	0.862

*M_T = the moment at the position of the mono-column face

filling.

- In the test, the interior joint failure modes included heaves and cracks in the end plates and local buckling and crack at the curved corners. Given that the end plate connection determined the integral seismic performance of the interior joint, the stiffness and peak bearing capacity of the interior joint specimens were reduced compared with the corner and exterior joint specimens.
- The hysteresis loops of all the specimens were plump with little noticeable pinching effect. The ductility factors were between 2.72 and 3.39. The maximum and minimum equivalent damping coefficients were 0.447 and 0.301, respectively, indicating good post-yielding deformation capacity and energy consumption capacity.
- According to the seismic behaviour of the joint, transverse steel plates in the L-CFST columns could be placed within 600 mm from the panel zone. By combining other mechanical test results of the L-CFST columns, the welding workload could be decreased significantly by reducing the number of transverse steel plates, which was conducive to industrial popularization and applications of these structural systems.
- The L-CFST column structural system composed of these types of connections belongs to the IMF category. These connections can also be used in high-rise steel structure residential buildings by adopting braces, shear walls or reinforced concrete cores to support a large share of the lateral load.
- In a comparison of experimental results, the results of the proposed calculation methods exhibited excellent agreement with the experimental results for both yield and ultimate flexural capacity for the end connection in the interior joint.

The test results in this paper are significant for the study of the joints in the L-CFST structural system which is applicable to high-rise steel structure houses. These results supply an experimental basis for follow-up optimization design and finite element numerical calculations.

Acknowledgments

This work was sponsored by the National Key Research and Development Program of China (Grant No. 2017YFC0703802) and the Key Project of Hebei Natural Science Foundation, China (Grant No. E2017202278).

References

AISC 341-05 (2005), Seismic provisions for structural steel buildings, American Institute of Steel Construction, Chicago, IL, USA.

Applied Technology Council (ATC) (2009), Effects of strength and stiffness degradation on the seismic response of structural systems, Report No. FEMA P440A, Washington, DC, USA.

Chopra, A. (2005), *Dynamics of Structures*: *Theory and Applications to Earthquake Engineering*, (2nd Edition), Pearson/Prentice Hall.

CEB-FIPMC-90 (1993), Model code for concrete structures, Comité Euro International du Beton- Fédération International de la Précontrainte, Paris, France.

Chung, J., Seo, S., Matsui, C. and Choi, S. (2005), "Hysteresis Behavior of Square Tube Columns to H-Beam Connections with Side plates", *Adv. Struct. Eng.*, **8**(6), 561-572.

Fardis, M.N. and Panagiotakos, T.B. (1997), "Seismic design and response of bare and masonry-infilled, reinforced concrete buildings part ii: Infilled structures", *J. Earthq. Eng.*, **1**(3), 475-503.

GB50017-2003 (2003), Code for design of steel structures, China Planning Press, Beijing, China.

Ghobadi, M.S., Ghassemieh, M., Mazroi, A. and Abolmaali, A. (2009a), "Seismic performance of ductile welded connections using T-stiffener", *J. Constr. Steel Res.*, **65**(4), 766-775.

Ghobadi, M.S., Mazroi, A. and Ghassemieh, M. (2009b), "Cyclic response characteristics of retrofitted moment resisting connections", *J. Constr. Steel Res.*, **65**(3), 586-598.

Jafarian, M. and Wang, Y.C. (2015), "Tying resistance of reverse channel connection to concrete filled square and rectangular tubular sections", *Eng. Struct.*, **100**, 17-30.

Jazany, R.A. and Ghobadi, M.S. (2017), "Design methodology for inclined continuity plate of panel zone", *Thin-Wall. Struct.*, **113**, 69-82.

Jazany, R.A. (2017), "Improved design of drilled flange (DF) moment resisting connection for seismic regions", *Bull. Earthq. Eng.*, 1-34.

JGJ101-96 (1997), Specification of testing methods for earthquake Resistant building, China Architecture & Building Press, Beijing, China.

Kang, C.H., Kim, Y.J., Shin, K.J. and Oh, Y.S. (2013), "Experimental investigation of composite moment connections with external stiffeners", *Adv. Struct. Eng.*, **16**(10), 1683-1700.

Kang, L., Leon, R.T. and Lu, X. (2015), "Shear strength analyses of internal diaphragm connections to CFT columns", *Steel Compos. Struct., Int. J.*, **18**(5), 1083-1101.

Lee, S.H., Yang, I.S. and Choi, S.M. (2010), "Structural characteristics of welded built-up square CFT column-to-beam connections with external diaphragms", *Steel Compos. Struct., Int. J.*, **10**(3), 261-279.

Ma, R.Q., Ban, H.Y., Zhao, Y.Z., Wang, Y.Q., Li, Q. and Liu, M. (2017), "Experimental study on seismic behavior of steel beam to wide-flange specially-shaped composite column connections", *J. Build. Struct.*, **38**(6), 105-111. [In Chinese]

Mehr, S.M.R.F. and Ghobadi, M.S. (2017), "Seismic performance of retrofitted WFP connections joined to box column using ribs", *J. Constr. Steel Res.*, **137**, 297-310.

Nie, J., Qin, K. and Cai, C.S. (2009), "Seismic behavior of composite connections - flexural capacity analysis", *J. Constr. Steel Res.*, **65**(5), 1112-1120.

Rezaifar, O. and Younesi, A. (2016), "Finite element study the seismic behavior of connection to replace the continuity plates in (NFC/CFT) steel columns", *Steel Compos. Struct., Int. J.*, **21**(1), 73-91.

Qin, Y., Chen, Z.H. and Rong, B. (2014), "Component-based mechanical models for axially-loaded through-diaphragm connections to concrete-filled RHS columns", *J. Constr. Steel Res.*, **102**(11), 150-163.

Qin, Y., Chen, Z.H., Bai, J.J. and Li, Z.L. (2016), "Test of extended thick-walled through-diaphragm connection to thick-walled CFT column", *Steel Compos. Struct., Int. J.*, **20**(1), 1-20.

Rong, B., Liu, R., Zhang, R.Y., Chen, Z.H. and Apostolos, F. (2016), "Flexural bearing capacity of diaphragm-through joints of concrete-filled square steel tubular columns", *Steel Compos. Struct., Int. J.*, **20**(3), 487-500.

Shin, K.J., Kim, Y.J., Oh, Y.S. and Moon, T.S. (2004), "Behavior of welded CFT column to H-beam connections with external stiffeners", *Eng*. *Struct*., **26**(13), 1877-1887.

Shin, K.J., Kim, Y.J. and Oh, Y.S. (2008), "Seismic behaviour of composite concrete-filled tube column-to-beam moment connections", *Steel Constr*., **64**(1), 118-127.

Vulcu, C., Stratan, A., Ciutina, A. and Dan, D. (2017), "Beam-to-CFT high-strength joints with external diaphragm. I: Design and experimental validation", *J*. *Struct*. *Eng*., **143**(5), 04017001.

Xiong, Q.Q, Chen, Z.H., Kang, J.F., Zhou, T. and Zhang, W. (2017), "Experimental and finite element study on seismic performance of the LCFST-D columns", *J*. *Constr*. *Steel Res*., **137**, 119-134.

Zhao, B.Z., Zhou, T., Chen, Z.H., Yu, J.H., Yan, X.Y, Zheng, P.Z. and Zhao Z.W. (2017), "Experimental seismic behavior of SCFRT column chevron concentrically braced frames", *J*. *Constr*. *Steel Res*., **133**, 141-155.

Zhou, T., Jia, Y.M., Xu, M.Y., Wang, X.D. and Chen, Z.H. (2015), "Experimental study on the seismic performance of L-shaped column composed of concrete-filled steel tubes frame structures", *J*. *Constr*. *Steel Res*., **114**, 77-88.

CC